This is a non-peer reviewed EarthArXiv preprint version that has been submitted for publication in IEEE Trans. Geosci. and Remote Sens.

Instantaneous State InSAR: Smoothness Doublet and Ambiguity Resolution

Yuqing Wang and Ramon F. Hanssen *Senior Member, IEEE*

***Abstract*—Instantaneous state InSAR (ISI) enables epoch-wise parameterization, estimation and prediction for the dynamic motion of individual scatterers in near real-time displacement monitoring. Yet, it introduces a coupling problem: the state prediction (time-update) and the integer ambiguity resolution of double-difference phase (measurement-update) depend on each other in a recursive loop. An inaccurate prediction can lead to an incorrect integer ambiguity number, that subsequently contaminates the state estimate and degrades every subsequent prediction. We analyze this coupling within the ISI framework and propose a two-step approach to address the problem. First, we represent the smoothness doublet of the time-update, i.e., the standard deviation and decorrelation time of the instantaneous velocity, with two physically interpretable metrics: the fractal dimension and the maximum absolute average velocity, and derive empirical relations between them, so that for a particular case study, the smoothness constraint can be introduced from prior physical expectations rather than by trial and error. Second, for the measurement-update, we propose a probabilistic ambiguity-resolution strategy that evaluates a small set of candidate integer ambiguities and assigns each a likelihood derived from the predicted-residual distribution.**

***Index Terms*—InSAR point scatterers, Kalman filter, smoothness constraints, ambiguity resolution, implicit phase unwrapping**

I. Introduction

Instantaneous State InSAR (ISI) has been introduced for recursive, near-real-time estimation of the instantaneous displacement and velocity of individual scatterers, allowing new SAR acquisitions to be incorporated without reprocessing the complete observation history [1]. Unlike conventional InSAR approaches that rely on a prescribed temporal functional model, ISI represents the displacement dynamics through a stochastic state-space formulation. However, the non-uniqueness of InSAR solutions, primarily arising from the unknown integer phase ambiguities associated with individual observations, necessitates the introduction of constraints on the temporal evolution of displacement [2], [3].

In conventional InSAR approaches, temporal constraints are commonly imposed implicitly through the choice of a functional model, such as constant velocity, low-order polynomials, or periodic functions. These models restrict the admissible displacement histories to a predefined class of functions. For example, a constant-velocity model assumes zero acceleration throughout the observation period, thereby precluding any temporal variations in velocity within the assumed model. Consequently, displacement signals that cannot be adequately represented by the selected functional model may be misrepresented, with deviations potentially attributed to measurement noise or excluded from the solution. This motivates the use of stochastic temporal models that can accommodate more general displacement dynamics while retaining sufficient constraints for parameter estimation and ambiguity resolution.

ISI introduces temporal constraints by modeling the instantaneous velocity as an exponentially autocorrelated, mean-reverting Ornstein–Uhlenbeck (OU) process [4]. The OU process is characterized by two parameters: the stationary standard deviation of the instantaneous velocity, σ_v, and its decorrelation time, τ_v. Together, these parameters constitute the *smoothness doublet*, (σ_v, τ_v). The parameter σ_v characterizes the magnitude of velocity fluctuations, whereas τ_v determines their temporal persistence. Unlike a random-walk velocity model, whose variance increases without bound over time [5], [6], the OU process has a finite stationary variance and an exponentially decaying temporal correlation. The smoothness doublet therefore provides a physically interpretable stochastic description of the expected displacement dynamics, allowing the temporal constraints to be adapted to the characteristics of the monitored object and the monitoring objective.

Within the recursive Kalman-filter formulation of ISI [7], the state estimate at each epoch is obtained through two coupled operations. The *time update* propagates the state estimate and its covariance from the previous epoch according to the stochastic model defined by the smoothness doublet. The *measurement update* incorporates the new SAR observation after resolving its unknown integer phase ambiguity. These operations are closely related: the smoothness doublet determines the predicted state distribution and thereby influences the probability distribution of the predicted phase residuals, which provides the basis for integer ambiguity resolution. If the assumed stochastic model does not adequately represent the actual displacement dynamics, the predicted phase distribution may become inconsistent with the observations, increasing the probability of incorrect ambiguity resolution. Moreover, an incorrectly resolved ambiguity may affect subsequent estimates because the updated state is propagated to the next epoch. The choice of the smoothness doublet is therefore relevant not only to the estimated displacement dynamics but also to the ambiguity-resolution performance of the recursive estimator.

This coupling introduces two important challenges. First, selecting appropriate values for σ_v and τ_v requires prior knowledge of the expected displacement dynamics, which may be difficult to quantify. Second, integer ambiguity resolution in InSAR is commonly formulated as a deterministic phase-

The authors are with the Department of Geoscience and Remote Sensing, Delft University of Technology, Delft, 2628 CN, The Netherlands (email: y.wang-29@tudelft.nl, r.f.hanssen@tudelft.nl).

unwrapping problem, for example by imposing a minimum-gradient assumption [8]. Such an approach does not explicitly account for the uncertainty of the predicted phase or evaluate the relative probabilities of alternative integer ambiguities. In a recursive state-space formulation, however, the predicted phase distribution provides information that can be exploited for probabilistic ambiguity resolution.

In this study, we address both challenges within the ISI framework. First, we investigate the relationship between the smoothness doublet and two empirical metrics describing displacement dynamics: the fractal dimension D_f and the maximum absolute average velocity $|\bar{v}_{\max}|$. These metrics serve as physically interpretable proxies for temporal roughness and the magnitude of displacement rates, respectively. We investigate how these metrics relate to the stochastic properties represented by the smoothness doublet, with the aim of providing physically interpretable guidance for selecting its parameters based on prior expectations of displacement behavior. Second, we introduce a probabilistic integer ambiguity-resolution strategy for the measurement update. Rather than selecting an ambiguity based on a deterministic minimum-gradient criterion, the proposed approach evaluates multiple candidate integer ambiguities and assigns likelihoods based on the predicted phase-residual distribution. This explicitly incorporates the uncertainty of the recursive state estimate into the ambiguity-resolution procedure.

The remainder of this paper is organized as follows. Section II summarizes the ISI state-space formulation and examines the coupled influence of the smoothness doublet and integer ambiguity resolution on recursive state estimation. Section III introduces the two empirical smoothness metrics and investigates their relationship with the smoothness doublet. Section IV develops the probabilistic integer ambiguity-resolution strategy. Section V evaluates the resulting ambiguity likelihoods using real data and discusses the influence of the smoothness doublet and measurement noise. Finally, Section VI presents the conclusions.

II. Coupling Between Smoothness Constraints and Ambiguity Resolution

In ISI, the smoothness doublet and integer ambiguity resolution jointly influence the estimated displacement dynamics. The smoothness doublet governs the stochastic evolution of the instantaneous state and its uncertainty, while integer ambiguity resolution determines how new modulo-2π phase observations are incorporated into the recursive estimator. This section summarizes the instantaneous-state formulation and examines the interaction between these two components.

A. Instantaneous State Estimation

We briefly summarize the instantaneous-state estimation framework underlying ISI; a complete derivation is provided in [1].

For a spatial arc connecting two coherent point scatterers, the instantaneous state at epoch t consists of two kinematic components: the instantaneous relative line-of-sight position p_t and its instantaneous velocity v_t, expressed in meters and meters per unit time, respectively. The state vector is defined as [1]

$$x_t = [p_t \; v_t]^{\mathsf{T}}. \tag{1}$$

The instantaneous velocity is modeled as a stationary Ornstein–Uhlenbeck process, characterized by the smoothness doublet (σ_v, τ_v). Here, σ_v denotes the stationary standard deviation of velocity, and τ_v its decorrelation time. These parameters jointly determine the temporal covariance structure of the displacement process.

The recursive estimation consists of a *time update* and a *measurement update*. During the time update, the state estimate and its covariance are propagated from epoch $t-1$ to epoch t through a state-transition model [9],

$$\underline{x}_t = \Phi_{t,t-1}\,\underline{x}_{t-1} + \underline{d}_t, \quad E\{\underline{d}\} = 0 \tag{2}$$

which leads to

$$\underline{\hat{x}}_{t|t-1} = \Phi_{t,t-1}\,\underline{\hat{x}}_{t-1|t-1}, \tag{3}$$

$$Q_{\hat{x}_{t|t-1}} = \Phi_{t,t-1}\,Q_{\hat{x}_{t-1|t-1}}\,\Phi_{t,t-1}^{\mathsf{T}} + Q_{\Delta t}, \tag{4}$$

Here, $\Phi_{t,t-1}$ denotes the 2×2 state-transition matrix, and $Q_{\hat{x}_{t|t-1}}$ is the predicted state-estimation error covariance. The process-noise (or *difference*) vector $\underline{d}_t$ represents the stochastic evolution of the state between consecutive epochs, with covariance $Q_{\Delta t}$. Both $\Phi_{t,t-1}$ and $Q_{\Delta t}$ depend on the smoothness doublet (σ_v, τ_v) and the elapsed time Δt.

The state transition matrix $\Phi_{t,t-1}$ can be expressed as [9]

$$\Phi_{t,t-1} = \begin{bmatrix} 1 & \tau_v\left(1 - e^{-\Delta t/\tau_v}\right) \\ 0 & e^{-\Delta t/\tau_v} \end{bmatrix}, \tag{5}$$

and $Q_{\Delta t}$ is given by [9]

$$Q_{\Delta t} = \sigma_v^2 \begin{bmatrix} q_{11} & q_{12} \\ q_{21} & q_{22} \end{bmatrix} \tag{6}$$

with

$$\begin{aligned} q_{11} &= 2\tau_v\Delta t - \tau_v^2\left(3 - 4e^{-\Delta t/\tau_v} + e^{-2\Delta t/\tau_v}\right), \\ q_{21} = q_{12} &= \tau_v\left(1 - e^{-\Delta t/\tau_v}\right)^2, \\ q_{22} &= \left(1 - e^{-2\Delta t/\tau_v}\right), \end{aligned} \tag{7}$$

where Δt indicates the absolute value of the time difference between epoch t and $t-1$, see [1] for the derivation of these components. Note that transition matrix $\Phi_{t,t-1}$ requires the decorrelation time τ_v as input, and $Q_{\Delta t}$ requires the smoothness doublet (σ_v, τ_v) as input.

Once the prediction $\underline{\hat{x}}_{t|t-1}$ is obtained, the *updated* state vector $\underline{\hat{x}}_{t|t}$ and its corresponding VCM $Q_{\hat{x}_{t|t}}$ can be computed by including the new observation

$$\phi_t^{(k)} = \phi_t^{\mathrm{w}} + 2\pi k_t, \quad k_t \in \mathbb{Z}, \tag{8}$$

where $\phi_t^{\mathrm{w}} \in [-\pi, +\pi) \subset \mathbb{R}$ denotes the modulo-2π phase observation, and $\phi_t^{(k)} \in \mathbb{R}$ the corresponding candidate absolute phase, conditional on the integer ambiguity k_t, using the *measurement-update equation* [9, p.217],

$$\underline{\hat{x}}_{t|t}^{(k)} = \underline{\hat{x}}_{t|t-1} + Q_{\hat{x}_{t|t}} A_t{}^{\mathsf{T}} Q_{\phi_t}^{-1} \left(\underline{\phi}_t^{(k)} - A_t \underline{\hat{x}}_{t|t-1} \right); \quad (9)$$

$$Q_{\hat{x}_{t|t}} = \left(Q_{\hat{x}_{t|t-1}}^{-1} + A_t{}^{\mathsf{T}} Q_{\phi_t}^{-1} A_t \right)^{-1}. \quad (10)$$

The updated covariance is conditional on the selected integer ambiguity and does not account for uncertainty associated with ambiguity resolution. The design matrix A_t is defined by

$$A_t = \begin{bmatrix} -\frac{4\pi}{\lambda} & 0 \end{bmatrix}, \quad (11)$$

where the first entry transforms the position p_t into radians. The second entry is null since the position is captured in p_t, while v_t is not relevant in the expectation of $\underline{\phi}_t^{(k)}$. The variance Q_{ϕ_t} of the phase observation is approximated by the normalized median absolute deviation of the amplitude [10]. The *updated state* estimate is obtained by combining the *predicted* state with the candidate absolute-phase observation. The contribution of the observation is governed by the Kalman gain, while the resulting state-estimation error covariance is conditional on the selected integer ambiguity. The *state correction* $\Delta\underline{\hat{x}}_{t|t-1}$ is determined by the second term on the right-hand side of Eq. (9), i.e.,

$$\Delta\underline{\hat{x}}_{t|t-1}^{(k)} = K_t \underline{e}_{t|t-1}^{(k)}, \text{where} \quad (12)$$

$$K_t = Q_{\hat{x}_{t|t}} A_t{}^{\mathsf{T}} Q_{\phi_t}^{-1}, \text{ and} \quad (13)$$

$$\underline{e}_{t|t-1}^{(k)} = \underline{\phi}_t^{(k)} - A_t \underline{\hat{x}}_{t|t-1}. \quad (14)$$

The Kalman gain K_t determines the contribution of the new observation to the updated state estimate, based on the predicted state covariance and the measurement-noise variance. Since the predicted covariance depends on the smoothness doublet (σ_v, τ_v), these parameters influence the measurement update. Moreover, the predicted phase residual $\underline{e}_{t|t-1}^{(k)}$ depends on the candidate integer ambiguity k_t. Consequently, the smoothness doublet and ambiguity resolution jointly influence the updated state estimate and, through recursive propagation, potentially affect subsequent estimates.

B. Influence of the Smoothness Doublet

The smoothness doublet (σ_v, τ_v) determines the stochastic properties of the instantaneous velocity and, consequently, influences the recursive state estimates. The stationary velocity standard deviation σ_v controls the magnitude of velocity fluctuations, whereas the decorrelation time τ_v determines their temporal persistence. The decorrelation time τ_v determines the state-transition matrix $\Phi_{t,t-1}$, while both parameters determine the process-noise covariance $Q_{\Delta t}$, which together govern the time update.

The two parameters influence the stochastic model differently. Increasing σ_v increases the process-noise covariance proportionally to σ_v^2, whereas changing τ_v modifies the temporal correlation structure. A large τ_v implies more persistent velocity fluctuations, while a small τ_v implies more rapid decorrelation. Consequently, the effect of the smoothness doublet on the predicted state covariance and Kalman gain cannot generally be classified as uniformly strong or weak. Table I summarizes the distinct influences of the two parameters.

Through the time update, the smoothness doublet influences the predicted state covariance $Q_{\hat{x}_{t|t-1}}$, which subsequently determines the Kalman gain K_t. The Kalman gain determines how the predicted phase residual is weighted in the measurement update. Consequently, different smoothness doublets may lead to different state corrections for the same phase observation, even when the selected integer ambiguity remains unchanged.

The smoothness doublet also influences integer ambiguity resolution. Since the predicted phase and its uncertainty depend on the assumed stochastic displacement model, different smoothness doublets may yield different predicted phase-residual distributions. These differences can affect the relative likelihoods of candidate integer ambiguities and, consequently, the selected ambiguity. An incorrect ambiguity may subsequently propagate through the recursive estimation, influencing later state estimates and ambiguity decisions.

The appropriate choice of the smoothness doublet therefore depends on the expected displacement dynamics and the monitoring objective. Applications involving slowly varying deformation may benefit from longer velocity correlation times, whereas applications requiring sensitivity to rapid changes may require shorter correlation times. The magnitude of the expected velocity fluctuations should be reflected in the choice of σ_v. Both parameters should be selected jointly, based on prior expectations of the monitored behavior, rather than interpreted as a single measure of smoothness strength.

C. Influence of Ambiguity Resolution

The selected integer ambiguity determines the candidate absolute-phase observation and, consequently, the predicted phase residual used in the measurement update. An incorrect ambiguity therefore introduces an error into the phase residual, which may affect the updated state estimate through the Kalman gain and propagate into subsequent epochs.

To quantify this effect, let k_t^* denote the correct integer ambiguity and $\hat{k}_t$ the selected ambiguity. Their difference is

$$\delta k_t = \hat{k}_t - k_t^* \in \mathbb{Z}. \quad (15)$$

An incorrect ambiguity introduces a phase offset of $2\pi\delta k_t$ into the candidate absolute-phase observation. For the same predicted state and Kalman gain, the resulting difference between the updated state estimates obtained with the selected and correct ambiguities is

$$\delta\underline{\hat{x}}_{t|t} = \underline{\hat{x}}_{t|t}^{(\hat{k}_t)} - \underline{\hat{x}}_{t|t}^{(k_t^*)} = 2\pi K_t \delta k_t. \quad (16)$$

This expression illustrates the interaction between ambiguity resolution and the smoothness doublet: the effect of an ambiguity error on the updated state depends on the Kalman gain, which is influenced by the assumed stochastic displacement model.

TABLE I: Qualitative influence of the smoothness doublet on instantaneous-state estimation. Comparisons assume fixed observation intervals, measurement-noise covariance, initial conditions, and the other smoothness parameter. Covariance comparisons use the positive-semidefinite ordering.

Parameter change	**Process-noise covariance** $Q_{\Delta t}$	**Predicted covariance** $Q_{\hat{x}_{t\|t-1}}$	**Kalman gain magnitude** $\|K_t\|$
Smaller σ_v	Decreases	Generally decreases	Generally smaller
Larger σ_v	Increases	Generally increases	Generally larger
Smaller τ_v	Component-dependent	Model-dependent	Model-dependent
Larger τ_v	Component-dependent	Model-dependent	Model-dependent

Two cases can be distinguished:

1) *Successful ambiguity resolution:* When $\hat{k}_t = k_t^*$, no ambiguity-induced phase offset is introduced. The predicted phase residual may still contain measurement noise and state-prediction errors, but the measurement update introduces no additional error attributable to ambiguity selection.
2) *Failed ambiguity resolution:* When $\hat{k}_t \neq k_t^*$, the selected phase differs from the correct candidate by $2\pi\delta k_t$. According to Eq. (16), this produces an ambiguity-dependent difference in the updated state estimate. Through subsequent time updates, this difference may affect later state estimates and ambiguity decisions. Its persistence depends on the filter dynamics and subsequent observations.

The ambiguity success probability, defined as $P_{\mathrm{s},t} = \Pr(\hat{k}_t = k_t^*)$, characterizes the probability of correct integer ambiguity selection at epoch t [11], [12]. However, this probability alone does not fully characterize the consequences of ambiguity resolution for state estimation. The magnitude and probability distribution of the ambiguity estimation errors also influence the recursive state estimates. This motivates an ambiguity-resolution strategy that accounts for the predicted phase distribution and its uncertainty.

D. Coupled Effects on State Estimation

The smoothness doublet and integer ambiguity resolution jointly influence instantaneous-state estimation through two mechanisms. First, the smoothness doublet influences the predicted state and its covariance, thereby affecting the predicted phase distribution used for ambiguity selection. Second, the predicted state covariance determines the Kalman gain, which governs the effect of an incorrect ambiguity on the updated state estimate.

To examine these interactions, we consider two contrasting configurations of the smoothness doublet: (i) a small stationary velocity standard deviation σ_v combined with a large decorrelation time τ_v, and (ii) a large σ_v combined with a small τ_v. The first configuration represents velocity fluctuations of relatively small magnitude and high temporal persistence, whereas the second represents larger fluctuations with more rapid temporal decorrelation. Their relative effects on the predicted state covariance and Kalman gain depend on the observation interval, the numerical values of both parameters, and the preceding estimation history. Consequently, neither configuration can universally be associated with a smaller or larger Kalman gain.

The influence on ambiguity selection can be characterized through the predicted phase-residual variance,

$$\sigma_{e,t}^2 = A_t Q_{\hat{x}_{t|t-1}} A_t^{\mathsf{T}} + \sigma_{\phi,t}^2, \tag{17}$$

where $\sigma_{e,t}$ is the standard deviation of the predicted phase residual and $\sigma_{\phi,t}^2$ is the phase-observation noise variance. Since neighboring integer ambiguity candidates differ by 2π, their statistical distinguishability depends on the *discrimination ratio*

$$\rho_t = \frac{2\pi}{\sigma_{e,t}}. \tag{18}$$

Under a correctly specified, unbiased Gaussian prediction model, a larger ρ_t indicates greater separation between neighboring integer ambiguity hypotheses relative to the predicted phase-residual uncertainty, favoring correct ambiguity selection. Conversely, a smaller ρ_t implies greater overlap between their probability distributions, making ambiguity discrimination less reliable. This interpretation assumes that the predicted phase is unbiased and that the stochastic model adequately represents the actual displacement dynamics.

The second mechanism concerns the consequences of incorrect ambiguity selection. As established in Eq. (16), an ambiguity error δk_t introduces a difference of $2\pi K_t \delta k_t$ into the updated state estimate. Thus, the same ambiguity error may have different effects under different smoothness doublets because the resulting Kalman gains differ. Correct ambiguity selection introduces no such ambiguity-induced error, regardless of the smoothness-doublet configuration.

Together, these mechanisms demonstrate that the smoothness doublet influences both the probability of correct ambiguity selection and the consequences of ambiguity errors. Reliable instantaneous-state estimation therefore requires an appropriate stochastic displacement model and an ambiguity-resolution strategy that accounts for the predicted phase uncertainty.

III. A Priori Specification of the Smoothness Doublet

The time update in ISI requires the smoothness doublet (σ_v, τ_v) to be specified a priori. These parameters represent assumptions about the expected displacement dynamics and should therefore be selected independently of the InSAR observations used in the recursive estimation. However, their

numerical values may be difficult to postulate directly, particularly for users who are more familiar with the physical behavior of the monitored object than with stochastic process parameters.

We therefore propose an alternative, more intuitive parameterization of the smoothness doublet using two metrics: the effective fractal dimension D_f, representing the expected temporal roughness of the displacement signal, and the maximum absolute average velocity $|\bar{v}_{\max}|$, representing a probabilistic bound on its average displacement rate over a specified period. Both metrics are intended to be postulated from a priori contextual information, physical expectations, or experience, rather than estimated from the InSAR observations.

Through analytical relationships and simulations of the assumed stochastic displacement model, we establish a mapping from these metrics to the smoothness doublet (σ_v, τ_v). This allows the stochastic constraints required by ISI to be specified either directly through the smoothness doublet or indirectly through more physically interpretable characteristics of the expected displacement behavior.

A. Effective Fractal Dimension

The fractal dimension D_f characterizes the geometric complexity of a time series and is commonly used to quantify temporal roughness [13], [14]. For a self-affine stochastic process, the fractal dimension of its graph is related to the Hurst exponent H, which describes how temporal fluctuations scale with the observation interval. A higher fractal dimension indicates more irregular temporal behavior, whereas a lower fractal dimension corresponds to a smoother trajectory.

The scaling behavior can be characterized through the theoretical semivariogram [15]

$$\gamma(\Delta t) = \frac{1}{2} E\{\big(p(t+\Delta t) - p(t)\big)^2\}, \tag{19}$$

where $p(t)$ denotes the relative position process and Δt is the temporal lag. For a process with stationary increments, the semivariogram depends only on Δt. A self-affine process exhibits power-law scaling over an appropriate range of temporal lags [13],

$$\gamma(\Delta t) \propto (\Delta t)^{2H}, \tag{20}$$

where H is the Hurst exponent [16]. For a one-dimensional self-affine time series with $0 < H < 1$, the graph fractal dimension is given by [13]

$$D_f = 2 - H. \tag{21}$$

The displacement process considered in ISI is obtained by integrating a stationary Ornstein–Uhlenbeck velocity process. Using the OU velocity covariance function [4]

$$C_v(u) = \mathrm{Cov}[v(t), v(t+u)] = \sigma_v^2 e^{-|u|/\tau_v}, \tag{22}$$

the theoretical displacement semivariogram becomes

$$\gamma(\Delta t) = \sigma_v^2 \tau_v \left[\Delta t - \tau_v \left(1 - e^{-\Delta t/\tau_v}\right)\right], \tag{23}$$

for $\Delta t \geq 0$. This expression shows that σ_v^2 acts as a multiplicative scale factor, whereas τ_v controls the shape of the semivariogram as a function of temporal lag.

The semivariogram exhibits two limiting scaling regimes:

$$\gamma(\Delta t) \approx \begin{cases} \frac{1}{2}\sigma_v^2 (\Delta t)^2, & \Delta t \ll \tau_v, \\ \sigma_v^2 \tau_v \Delta t, & \Delta t \gg \tau_v. \end{cases} \tag{24}$$

At short temporal lags, the quadratic scaling corresponds to $H = 1$, reflecting the locally smooth displacement trajectory. At long lags, the approximately linear scaling corresponds to an effective exponent $H = 1/2$. The transition between these regimes is governed by the decorrelation time τ_v.

Consequently, the integrated OU displacement process does not exhibit a single scaling exponent across all temporal scales. We therefore use D_f as an *effective fractal dimension*, characterizing the temporal roughness of the displacement signal over a prescribed range of temporal scales. Its value depends on the temporal sampling and the range of lags considered, rather than representing the theoretical graph dimension of the continuous-time displacement process.

In the proposed approach, the effective fractal dimension is postulated from a priori contextual information or experience concerning the expected displacement dynamics, rather than estimated from the InSAR observations. Its empirical relationship with τ_v is established through simulations in Section III.C, providing a physically interpretable alternative for specifying the decorrelation time required by ISI.

B. Probabilistic Bound on Average Velocity

The second metric used to specify the smoothness doublet is the maximum absolute average velocity, denoted by $|\bar{v}_{\max}|$. This metric provides a probabilistic bound on the magnitude of the average displacement rate over a prescribed period T. Unlike the stationary standard deviation of instantaneous velocity, σ_v, such a bound may be more readily postulated from prior knowledge of the expected displacement dynamics. The postulated bound is therefore associated with a specified averaging period T.

The average velocity over the period T is defined as

$$\bar{v} = \frac{1}{T}\int_0^T v(t)\,\mathrm{d}t = \frac{p(T) - p(0)}{T}, \tag{25}$$

where $v(t)$ and $p(t)$ denote the instantaneous velocity and relative position, respectively. Thus, $\bar{v}$ represents the net displacement divided by the duration of the observation period.

For a zero-mean, second-order stationary velocity process, the variance of the average velocity is [16]

$$\sigma_{\bar{v}}^2 = \frac{2}{T^2}\int_0^T (T-u) C_v(u)\,\mathrm{d}u, \tag{26}$$

where $C_v(u)$ denotes the velocity autocovariance function. Substituting the stationary OU covariance function in Eq. (22) into Eq. (26) and evaluating the integral yields

$$\sigma_{\bar{v}} = \sigma_v \sqrt{\frac{2\tau_v}{T}\left[1 - \frac{\tau_v}{T}\left(1 - e^{-T/\tau_v}\right)\right]}. \tag{27}$$

Two limiting cases illustrate the dependence on the observation period:

$$\sigma_{\bar{v}} \approx \begin{cases} \sigma_v, & T \ll \tau_v, \\ \sigma_v \sqrt{2\tau_v/T}, & T \gg \tau_v. \end{cases} \tag{28}$$

For observation periods much shorter than the decorrelation time, the velocity remains strongly correlated, and averaging provides little reduction in its standard deviation. Conversely, for periods much longer than the decorrelation time, temporal averaging increasingly reduces the contribution of velocity fluctuations, and $\sigma_{\bar{v}}$ decreases approximately as $T^{-1/2}$.

Because the average velocity is a linear functional of a zero-mean Gaussian process, it is itself normally distributed with zero mean and standard deviation $\sigma_{\bar{v}}$. We define the maximum absolute average velocity as the two-standard-deviation bound,

$$|\bar{v}_{\max}| = 2\sigma_{\bar{v}} = 2\sigma_v \sqrt{\frac{2\tau_v}{T}\left[1 - \frac{\tau_v}{T}\left(1 - e^{-T/\tau_v}\right)\right]}, \tag{29}$$

such that $\Pr(|\bar{v}| \leq |\bar{v}_{\max}|) \approx 0.9545$. Hence, $|\bar{v}_{\max}|$ represents a probabilistic bound rather than an absolute maximum.

Introducing the dimensionless ratio $r = T/\tau_v$, Eq. (29) can be written as

$$|\bar{v}_{\max}| = 2\sigma_v \sqrt{\frac{2}{r}\left[1 - \frac{1}{r}(1 - e^{-r})\right]}. \tag{30}$$

This relationship shows that, for a prescribed observation period T, the maximum absolute average velocity depends on both components of the smoothness doublet. Consequently, postulating $|\bar{v}_{\max}|$ constrains a combination of σ_v and τ_v, but does not uniquely determine either parameter.

For $T \gg \tau_v$, Eq. (29) simplifies to

$$|\bar{v}_{\max}| \approx 2\sigma_v \sqrt{\frac{2\tau_v}{T}}, \qquad \sigma_{\bar{v}} \approx \sigma_v \sqrt{\frac{2\tau_v}{T}}. \tag{31}$$

Therefore, for a fixed T and a prescribed $|\bar{v}_{\max}|$,

$$\sigma_v^2 \tau_v \approx \text{constant}. \tag{32}$$

An additional assumption is thus required to specify both parameters independently. The effective fractal dimension introduced in Sec. III-A provides this complementary information by characterizing the expected temporal roughness. Its empirical relationship with τ_v, established in Sec. III-C, enables the decorrelation time to be specified independently of σ_v. Together, the postulated D_f and $|\bar{v}_{\max}|$ provide an alternative, physically interpretable parameterization of the smoothness doublet.

C. Calibration of Effective Fractal Dimension

To establish an empirical relationship between the effective fractal dimension D_f and the OU decorrelation time τ_v, we simulate displacement time series for prescribed smoothness doublets (σ_v, τ_v). The simulations are based on the time-update model in Eqs. (3) and (4), without additional observation noise.

The simulated displacement trajectories have a sampling interval of $\Delta t = 6$ days and a duration of ten years. We consider $\sigma_v \in \{1, 2, \ldots, 20\}$ mm/yr, and $\tau_v \in \{10, 20, \ldots, 360\}$ days. This yields 720 smoothness-doublet combinations. For each combination, we generate 100 independent realizations and calculate their effective fractal dimensions. For each realization, we calculate the empirical semivariogram at a prescribed set of temporal lags $\Delta t \in \{6, 12, \ldots, 90\}$ days and estimate an effective Hurst exponent from the slope of its logarithm as a function of logarithmic lag. The effective fractal dimension then follows from Eq. (21). The resulting values are averaged over the 100 realizations.

Fig. 1a shows that the effective fractal dimension is largely independent of σ_v, but decreases monotonically with increasing τ_v. This behavior is consistent with the theoretical semivariogram in Eq. (23): σ_v^2 acts as a multiplicative scale factor, whereas τ_v controls the transition between the temporal scaling regimes. Consequently, the effective fractal dimension primarily reflects the decorrelation time rather than the magnitude of velocity fluctuations.

To investigate the influence of simulation duration, we repeat the experiment for $T \in \{2, 4, 6, 8, 10\}$ years. The resulting relationships between D_f and τ_v are shown in Fig. 1d. The two-year simulations yield systematically higher effective fractal dimensions than the longer simulations, particularly at larger decorrelation times. The results for durations of four to ten years show closer agreement, suggesting that the empirical relationship becomes less sensitive to simulation duration over this range.

The resulting relationship between the effective fractal dimension and the decorrelation time can be approximated by

$$D_f(\tau_v) = \theta_1 \cdot (\tau_v + \theta_2)^{-1} + D_e, \tag{33}$$

where $D_e = 1$ denotes the dimension of the temporal domain, and $\theta_1 = 7$ days and $\theta_2 = 13$ days are empirically fitted coefficients, rounded for simplicity. The fitted model is shown in Fig. 1b, while Fig. 1c presents the differences between the simulated and modeled effective fractal dimensions. The small discrepancies indicate that Eq. (33) adequately approximates the simulated relationship over the investigated range of decorrelation times.

Equation (33) provides a practical mapping from a postulated effective fractal dimension to the OU decorrelation time. Thus, τ_v can be specified either directly from prior expectations of velocity persistence or indirectly through the expected temporal roughness represented by D_f. The calibration coefficients are specific to the adopted simulation settings and fractal-dimension estimation procedure.

D. Simulation-Based Validation of the Average-Velocity Bound

We simulate 100 time series of instantaneous velocities and their corresponding instantaneous positions for each combination of $\sigma_v \in \{1, 2, \ldots, 10\}$ mm/yr and $\tau_v \in \{30, 60, \ldots, 360\}$ days. We show an example velocity time series for the selected combinations of $\sigma_v \in \{1, 10\}$ mm/yr and $\tau_v \in \{30, 150, 360\}$ days in Fig. 2, and 50 position time series for the same combinations (100 for each subplot) in Fig. 3.

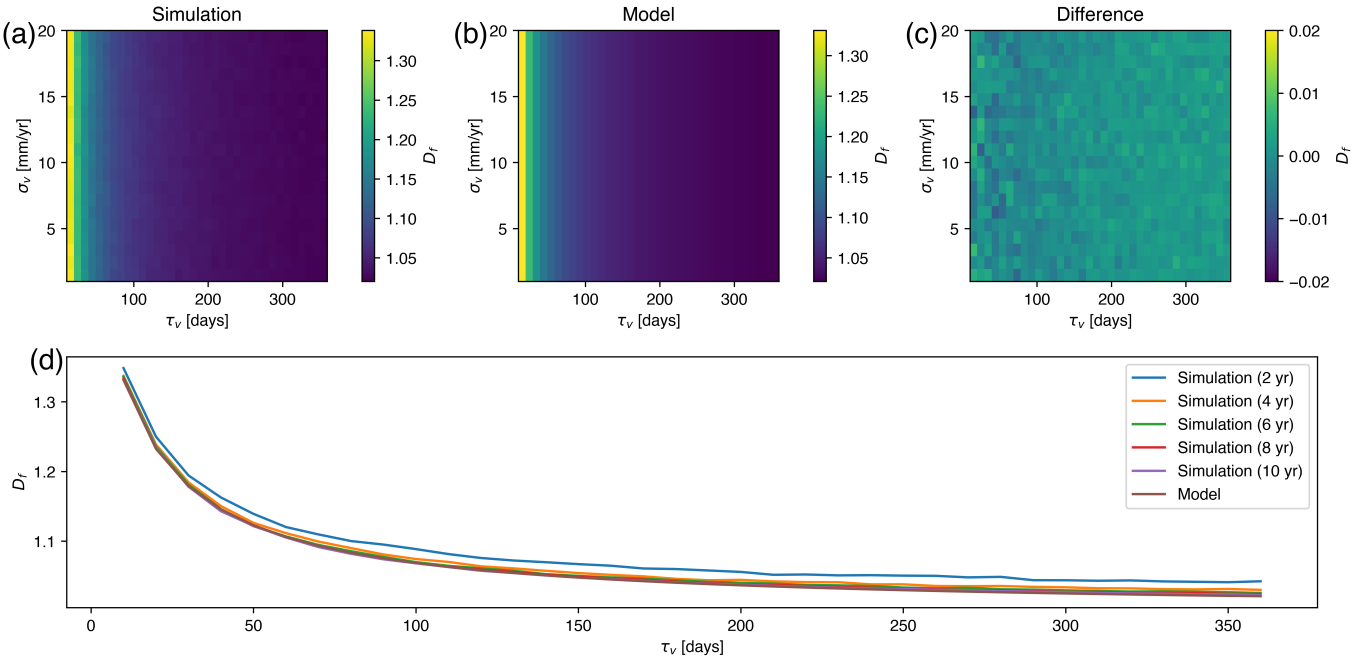


Fig. 1: Empirical relationship between effective fractal dimension D_f and OU decorrelation time τ_v. (a) Mean effective fractal dimension of simulated ten-year displacement trajectories for $\sigma_v \in \{1, 2, \ldots, 20\}$ mm/yr and $\tau_v \in \{10, 20, \ldots, 360\}$ days. (b) Empirical model fitted using Eq. (33). (c) Difference between simulated and modeled effective fractal dimensions. (d) Dependence of the effective fractal dimension on decorrelation time for simulation durations of 2, 4, 6, 8, and 10 years, together with the empirical calibration based on the ten-year simulations.

In Fig. 2, the left (blue) and right (red) axes show example time series of instantaneous velocity v for $\sigma_v = 1$ mm/yr and $\sigma_v = 10$ mm/yr, respectively, demonstrating that the range of possible average velocities scales with σ_v. The dashed lines indicate the pointwise 95.45% probability interval, $\pm 2\sigma_v$, for the stationary instantaneous velocity. Increasing σ_v increases the magnitude of velocity fluctuations, whereas increasing τ_v increases their temporal persistence, becoming progressively smoother. This smoother behavior propagates into the position time series, see Fig. 3, resulting in a larger range of possible average velocities, as indicated in the lower-left corner of each subplot. Thus, the range of possible average velocities increases with increasing σ_v and τ_v.

We then compute D_f and $|\bar{v}_{\max}|$ for the corresponding position time series. For each subplot in Fig. 3, the D_f is the same for $\sigma_v = 1$ mm/yr (left axis in blue) and $\sigma_v = 10$ mm/yr (right axis in red), which indicates that D_f is unrelated to σ_v. In Fig. 3a, when $D_f = 1.17$, i.e., $\tau_v = 30$ days, the signals appear rough and highly fluctuating, which is considered unrealistic for most InSAR time series signals in the built environment. In contrast, when $D_f = 1.05$, i.e., $\tau_v = 150$ days, see Fig. 3b, the signals are smoother and exhibit more realistic levels of fluctuation, and when $D_f = 1.02$, i.e., $\tau_v = 360$ days, see Fig. 3c, the signals are relatively smooth and closely resemble a steady-state linear trend.

Therefore, D_f decreases only with increasing τ_v, whereas the range of possible average velocities increases with increasing σ_v (comparing the left and right axes) and/or τ_v. Note that *high* values of (σ_v, τ_v) do not imply that the average velocity *will* be high, it is only that higher average velocities are more likely. Conversely, postulating small values of σ_v and τ_v reduces the variance of the average velocity over a fixed period T, thereby assigning lower probabilities to large net displacements. The smoothness doublet thus constrains the solution probabilistically rather than imposing a deterministic limit.

Figure 4 compares the maximum absolute average velocity obtained from the simulated displacement trajectories with the analytical relationship in Eq. (29). The close agreement confirms the predicted dependence on σ_v and τ_v for a fixed averaging period T, supporting the use of the analytical expression to specify the velocity variability from a prescribed probabilistic bound.

E. Mapping the Smoothness Metrics to the Smoothness Doublet

The effective fractal dimension D_f and maximum absolute average velocity $|\bar{v}_{\max}|$ provide an alternative, physically interpretable parameterization of the smoothness doublet. Both metrics are postulated a priori from contextual information and expectations of the displacement dynamics, rather than estimated from the InSAR observations. Given these metrics and a prescribed averaging period T, the smoothness doublet (σ_v, τ_v) can be determined sequentially.

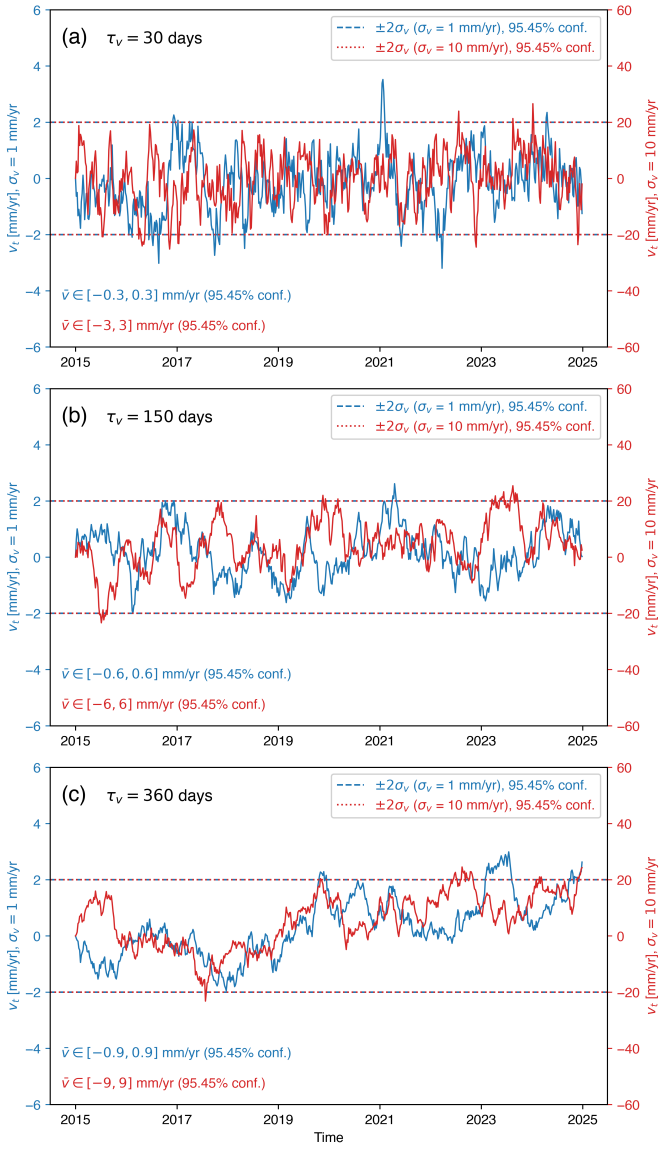


Fig. 2: Simulated instantaneous velocity time series for $\sigma_v \in \{1, 10\}$ mm/yr and $\tau_v \in \{30, 150, 360\}$ days. Left and right axes refer to $\sigma_v = 1$ and 10 mm/yr, in blue and red, respectively. The range of the possible average velocities is indicated in the lower-left corner and scales with σ_v. Dashed lines denote the 95.45% probability interval ($\pm 2\sigma_v$). Average velocities increase with σ_v and τ_v.

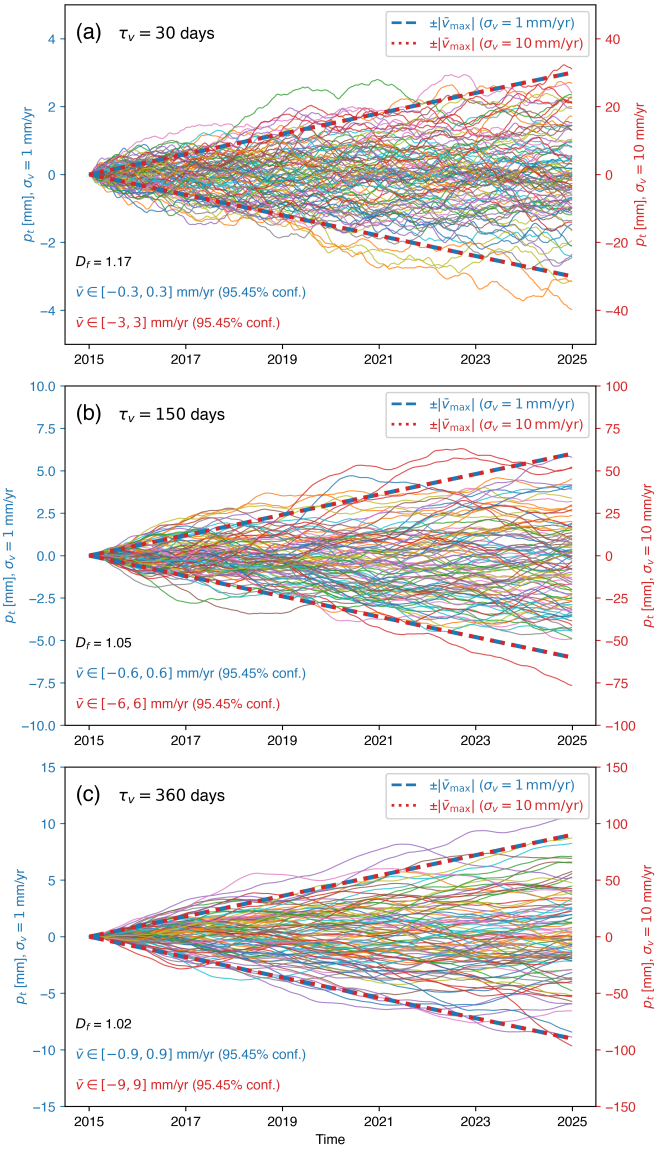


Fig. 3: Simulated position time series (100 for each subplot) for $\sigma_v \in \{1, 10\}$ mm/yr and $\tau_v \in \{30, 150, 360\}$ days. Left and right position axes refer to the cases with $\sigma_v = 1$ and 10 mm/yr, in blue and red, respectively. The fractal dimension D_f and the range of possible average velocities are indicated in the lower-left corner. Dashed lines denote the proposed bounds on the absolute average velocity, $\pm|\bar{v}_{\max}|$, representing the 95.45% probability interval. The fractal dimension D_f decreases with increasing τ_v, while average velocities increase with both σ_v and τ_v.

First, inverting the empirical relationship in Eq. (33), yields the OU decorrelation time

$$\tau_v = \theta_1 (D_f - D_e)^{-1} - \theta_2, \tag{34}$$

where $D_e = 1$. This mapping is valid within the range of the simulation-based calibration described in Sec. III-C.

Next, substituting the resulting τ_v into the analytical relationship in Eq. (29) gives the stationary velocity standard deviation

$$\sigma_v = \frac{|\bar{v}_{\max}|}{2} \sqrt{\frac{T}{2\tau_v \left[1 - \frac{\tau_v}{T}(1 - e^{-T/\tau_v})\right]}}. \tag{35}$$

Introducing the *normalized averaging interval* $r = T/\tau_v$, the

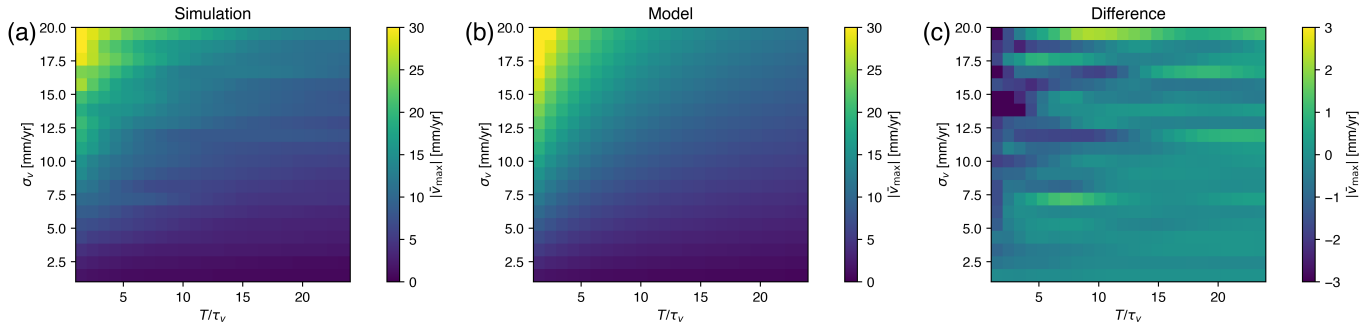


Fig. 4: (a) Range of the maximum absolute average velocity $|\bar{v}_{\max}|$ derived from the simulated displacement for $\sigma_v = [1, 10]$ mm/yr and $T/\tau_v = [1, 25]$, shown with a 95.45% probability interval. When T is fixed, the average velocity increases with increasing σ_v or τ_v, with both contributing positively. (b) The fitted model for the simulation with Eq. (30). (c) The difference between the simulation and the model.

stationary velocity standard deviation can be expressed as

$$\sigma_v = \frac{|\bar{v}_{\max}|}{2} \sqrt{\frac{r}{2\left[1 - r^{-1}(1 - e^{-r})\right]}}. \tag{36}$$

Thus, the postulated effective fractal dimension determines τ_v, while the probabilistic average-velocity bound, together with the prescribed averaging period, determines σ_v. The former mapping is empirical and depends on the adopted simulation and fractal-dimension estimation settings; the latter follows analytically from the stationary Ornstein–Uhlenbeck model.

This procedure allows the stochastic smoothness constraints required by ISI to be specified using physically interpretable prior expectations, while keeping their specification independent of the InSAR observations subsequently used for recursive estimation.

IV. Probabilistic Ambiguity Resolution

The smoothness doublet influences the predicted state and its uncertainty through the time update. As established in Sec. II, integer ambiguity resolution also affects the recursive estimation by determining the absolute-phase observation used in the measurement update. In this section, we develop a likelihood-based approach for selecting integer ambiguities using the predicted phase distribution.

If the absolute double-difference (DD) phase $\phi_t \in \mathbb{R}$ were known, the measurement update in Eq. (9) could be applied directly. However, the observed DD phase $\underline{\phi}_t^w \in [-\pi, \pi)$ is wrapped modulo-2π. The candidate absolute phase corresponding to an integer ambiguity $k_t \in \mathbb{Z}$ is therefore

$$\underline{\phi}_t^{(k)} = \underline{\phi}_t^w + 2\pi k_t. \tag{37}$$

For a given candidate ambiguity, the predicted phase residual is

$$\underline{e}_{t|t-1}^{(k)} = \underline{\phi}_t^{(k)} - \underline{\hat{\phi}}_{t|t-1}, \tag{38}$$

where the predicted phase is

$$\underline{\hat{\phi}}_{t|t-1} = A_t \underline{\hat{x}}_{t|t-1}. \tag{39}$$

The predicted phase residual provides the basis for evaluating the likelihood of each candidate integer ambiguity.

Under the assumed linear–Gaussian state-space model, and conditional on a correctly resolved ambiguity history, the predicted phase residual follows a zero-mean Gaussian distribution,

$$e_{t|t-1} \sim \mathcal{N}(0, \sigma_{e,t}^2), \tag{40}$$

where the predicted residual variance, as derived in Eq. (17), is

$$\sigma_{e,t}^2 = A_t Q_{\hat{x}_{t|t-1}} A_t^{\mathsf{T}} + \sigma_{\phi,t}^2. \tag{41}$$

The corresponding probability density function (PDF) is

$$p(e) = \frac{1}{\sqrt{2\pi}\sigma_{e,t}} \exp\left(-\frac{e^2}{2\sigma_{e,t}^2}\right). \tag{42}$$

The residual variance reflects both the uncertainty of the predicted state and the phase-observation noise. The Gaussian model is consistent with the linear-Gaussian assumptions underlying the Kalman filter. However, unmodeled displacement dynamics, phase decorrelation, or previous ambiguity errors may cause the actual residual distribution to deviate from this model.

When the integer ambiguity is unknown, each candidate absolute phase corresponds to a different predicted phase residual. The smoothness doublet constrains the predicted state and its uncertainty, thereby providing probabilistic information for distinguishing among candidate ambiguities. Rather than relying solely on a minimum-gradient criterion, we evaluate candidate ambiguities using the predicted residual distribution.

As illustrated in Fig. 5, adjacent integer ambiguities correspond to candidate predicted phase residuals separated by 2π. We associate each candidate k_t with a half-open interval of width 2π, centered on its predicted residual $e_{t|t-1}^{(k)}$. These resulting intervals are contiguous and non-overlapping.

The Gaussian probability mass associated with candidate k_t is defined as

$$\begin{aligned} P_t^{(k)} &= \Pr\left(e_{t|t-1} \in \left[e_{t|t-1}^{(k)} - \pi,\, e_{t|t-1}^{(k)} + \pi\right)\right) \\ &= \int_{e_{t|t-1}^{(k)}-\pi}^{e_{t|t-1}^{(k)}+\pi} p(e)\, de. \end{aligned} \tag{43}$$

The *interval probability* $P_t^{(k)}$ represents the probability mass of the predicted phase-residual distribution within the 2π-wide interval centered on the residual associated with candidate integer ambiguity k. The intervals associated with consecutive integers are contiguous and non-overlapping, and their probabilities sum to unity over all integer candidates. These probabilities quantify the support assigned to the respective residual intervals under the assumed stochastic model; they are not posterior probabilities of the integer ambiguities conditional on the observed wrapped phase.

For computational efficiency, we restrict the candidate search to the vicinity of the predicted phase. Defining

$$a_t = \frac{\hat{\phi}_{t|t-1} - \phi_t^w}{2\pi}, \tag{44}$$

the two adjacent candidate ambiguities are

$$k_t^{(1)} = \lfloor a_t \rfloor, \qquad k_t^{(2)} = \lceil a_t \rceil. \tag{45}$$

These correspond to the candidate absolute phases immediately below and above the predicted phase. If a_t is an integer, the prediction coincides with a candidate absolute phase, and the two expressions yield the same integer. Additional neighboring candidates can be included when required.

For each candidate, the predicted phase residual follows from Eq. (38), and its associated interval probability is calculated using Eq. (43). The selected integer ambiguity is

$$\hat{k}_t = \underset{k_t \in \mathcal{K}_t}{\arg\max;}\, P_t^{(k)}, \tag{46}$$

where $\mathcal{K}_t$ denotes the set of evaluated integer candidates.

Under the assumed centered Gaussian distribution, maximizing the interval probability is equivalent to selecting the candidate with the smallest absolute predicted phase residual. The predicted residual variance therefore does not change the selected ambiguity for a fixed predicted phase, but determines the probability masses assigned to the competing candidates.

As illustrated in Fig. 6, the blue and red shaded areas represent the probability masses associated with two neighboring candidate residuals. The interval centered closer to zero receives the larger probability mass. A smaller predicted residual standard deviation $\sigma_{e,t}$ generally produces a stronger concentration of probability mass around the candidate nearest to zero, whereas a larger $\sigma_{e,t}$ distributes probability mass across a wider range of candidate intervals.

Once the integer ambiguity has been selected, the corresponding predicted residual is

$$\hat{\underline{e}}_{t|t-1} = \underline{e}_{t|t-1}^{(\hat{k}_t)}, \tag{47}$$

and the selected absolute phase is

$$\hat{\underline{\phi}}_t = \hat{\underline{\phi}}_t^{(\hat{k}_t)} = \phi_t^w + 2\pi\hat{k}_t = \hat{\phi}_{t|t-1} + \hat{e}_{t|t-1}. \tag{48}$$

The selected absolute-phase observation is subsequently incorporated into the Kalman measurement update through the corresponding predicted residual,

$$\hat{\underline{x}}_{t|t} = \hat{\underline{x}}_{t|t-1} + K_t \hat{\underline{e}}_{t|t-1}, \tag{49}$$

where K_t denotes the Kalman gain defined in Sec. II. Thus, the selected integer ambiguity directly determines the correction applied to the predicted state, while the smoothness doublet influences both the predicted state and the Kalman gain through the time update.

The proposed approach integrates integer ambiguity resolution and recursive state estimation through the predicted phase and its uncertainty. The interval probabilities provide a quantitative indication of the support assigned to competing ambiguity candidates under the assumed stochastic model. When several candidates receive appreciable probability mass, additional candidates may be evaluated or retained for subsequent assessment. Multiple-hypothesis propagation, however, is beyond the scope of the present implementation.

V. Results and Discussion

The probabilistic ambiguity-resolution approach developed in Sec. IV assigns Gaussian probability mass to the residual interval associated with each candidate integer ambiguity. These probabilities depend on the candidate predicted phase residual and its variance, which are influenced by the postulated smoothness doublet and the phase-observation noise. In this section, we investigate how alternative ambiguity selections affect the resulting ISI solutions and examine the influence of the smoothness doublet on the associated interval probabilities.

A. Recursive Ambiguity Decisions and Solution Bifurcations

In ISI, integer ambiguity resolution is performed recursively as each new SAR acquisition becomes available. At epoch t, the ambiguity decision is based exclusively on the current observation and the state predicted from observations acquired up to epoch $t-1$. Future observations are unavailable and cannot contribute to the decision. Although Figs. 7 and 8 display complete time series, they must therefore be interpreted as sequences of individual decisions made without knowledge of subsequent observations. The encircled r in each panel emphasizes this retrospective interpretation of the recursive estimation process: the results are displayed retrospectively, but the decisions themselves were made using only information available at the respective epochs.

At a given epoch, multiple integer ambiguities may be compatible with the current wrapped phase observation and the predicted state, particularly when the prediction uncertainty is large or the displacement dynamics deviate from the assumed model. Selecting different ambiguities can produce distinct updated states and, consequently, different predictions at subsequent epochs. We refer to this divergence of alternative estimated trajectories as *bifurcation*. Each branch represents a

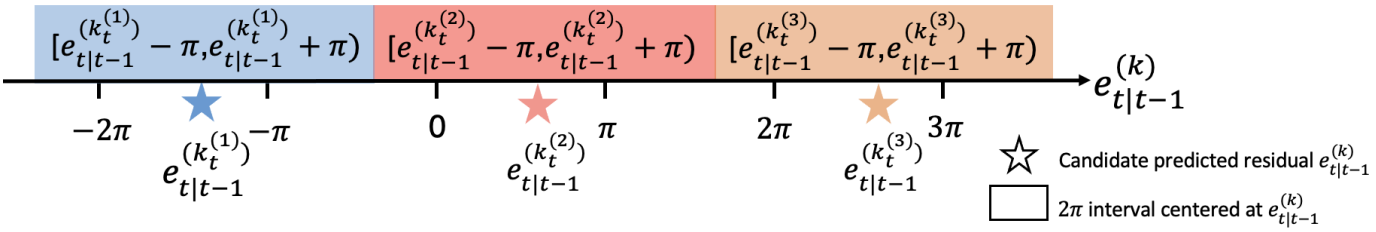


Fig. 5: Candidate predicted phase residuals $e_{t|t-1}^{(k)}$ (stars) and their associated half-open intervals $[e_{t|t-1}^{(k)} - \pi, e_{t|t-1}^{(k)} + \pi)$. Adjacent candidates are separated by 2π, and their intervals are contiguous and non-overlapping. The predicted residual distribution is centered at zero under the assumed linear–Gaussian model.

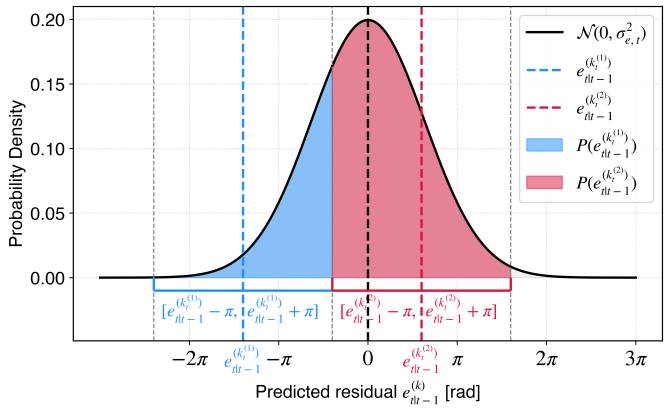


Fig. 6: Schematic representation of the Gaussian predicted phase-residual distribution and the intervals associated with two neighboring ambiguity candidates. The blue and red shaded areas indicate the probability masses assigned to the respective candidate intervals. The candidate whose residual is closest to zero receives the larger interval probability, under the assumed centered Gaussian model.

different sequence of ambiguity decisions, characterized by the interval probabilities introduced in Sec. IV.

Figure 7 illustrates this behavior for an arc between two real scatterers, using different smoothness doublets and ambiguity selections. The left column shows the resulting absolute-phase solutions and the interval probabilities associated with the selected ambiguities. The right column presents the corresponding selected predicted phase residuals $\hat{e}_{t|t-1}$, together with the pointwise 95.45% probability intervals, $\pm 2\sigma_{e,t}$, under the assumed Gaussian model.

The observations exhibit pronounced temporal phase changes between mid-2017 and mid-2018. During this period, the selected interval probabilities decrease at several epochs, indicating reduced agreement between the candidate absolute-phase observations and their predictions. At most other epochs, the selected candidates receive probability masses close to unity. Importantly, these probabilities are evaluated using the predictions available at each epoch, without knowledge of whether subsequent observations will confirm or contradict the selected ambiguity.

In Fig. 7a, the postulated smoothness doublet is $(\sigma_v, \tau_v) = (0.1, 90)$, with units of mm/yr and days, respectively, representing a relatively restrictive motion model. The resulting solution exhibits a smooth temporal evolution but does not closely follow the observed phase variability between mid-2017 and mid-2018. Consequently, larger predicted phase residuals occur, accompanied by lower interval probabilities at several epochs.

The remaining four solutions use a fixed smoothness doublet, $(\sigma_v, \tau_v) = (10, 30)$, but differ in their integer ambiguity selections. These alternative selections produce four distinct solution branches, highlighted in red. The dashed vertical lines indicate the two principal bifurcation epochs, in mid-2017 and mid-2018. At each bifurcation, the competing ambiguity candidates are evaluated using the information available at that epoch. The resulting branches are propagated independently, without using future observations to revise earlier decisions.

Figure 8 compares the five solutions. At the first bifurcation, in mid-2017, Solutions 1, 2, and 3 follow the upper branch, whereas Solutions 4 and 5 follow the lower branch. The interval probabilities are approximately 0.6 for Solution 1, 0.9999 for Solutions 2 and 3, and 0.0001 for Solutions 4 and 5. Thus, under their corresponding prediction models, Solutions 2 and 3 strongly favor the selected candidate, whereas Solutions 4 and 5 represent alternative ambiguity hypotheses rather than outcomes of the maximum-probability selection rule.

At the second bifurcation, in mid-2018, Solutions 2 and 4 select the lower-probability candidate. The corresponding interval probabilities for Solutions 1–5 are approximately 0.99995, 0.46, 0.54, 0.48, and 0.52, respectively. Except for Solution 1, these probabilities are relatively close to 0.5, indicating weaker discrimination between neighboring ambiguity candidates. This may be associated with increased predicted residual uncertainty following the earlier phase change, differences in the candidate residuals, or a combination of both. Crucially, the ambiguity selection at this epoch cannot exploit the subsequent evolution of the trajectories, even though that evolution is visible in Fig. 8.

The alternative solutions demonstrate how an ambiguity decision at one epoch affects subsequent state predictions and ambiguity selections. The complete trajectories reveal differences that could not have been anticipated when the

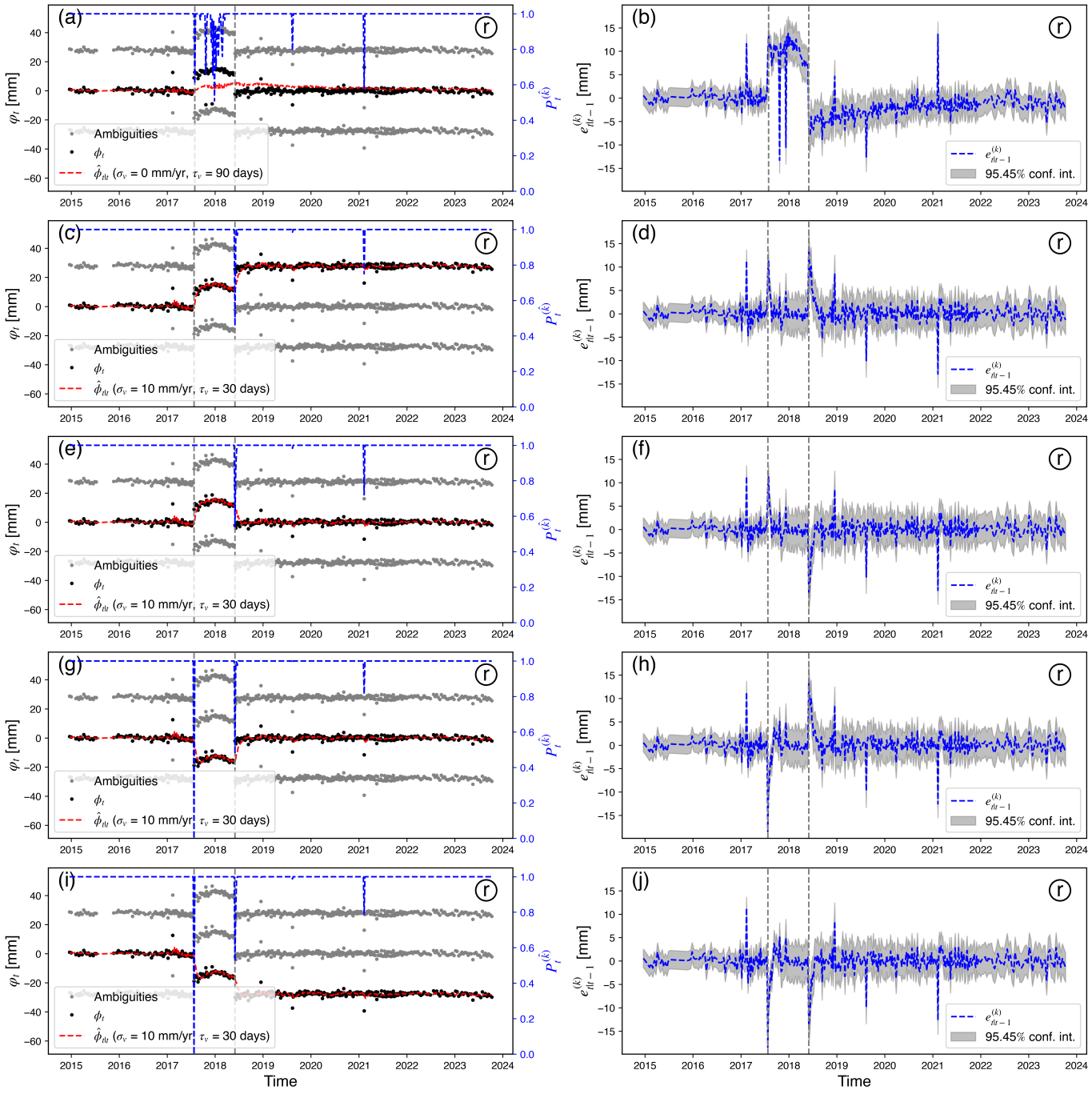


Fig. 7: Five alternative ISI solutions obtained from the same wrapped double-difference phase observations, using different postulated smoothness doublets and integer ambiguity selections. Rows 1–5 correspond to Solutions 1–5, respectively. The left column shows the absolute-phase observations and updated phase estimates, together with the interval probabilities $P_t^{(\hat{k})}$ associated with the selected ambiguities (blue, right axis). The right column shows the corresponding selected predicted phase residuals $e_{t|t-1}^{(k)}$ and their pointwise 95.45% prediction intervals, $\pm 2\sigma_{e,t}$, under the assumed Gaussian model. The applied smoothness doublet is specified in each left-panel legend. Vertical dashed lines indicate the two principal bifurcation epochs in mid-2017 and mid-2018. The alternative trajectories illustrate how different ambiguity selections influence subsequent state estimates. The circled lowercase r ⓡ indicates retrospective values, i.e., quantities that depend only on past and present data [1]. This symbol is adopted hereinafter.

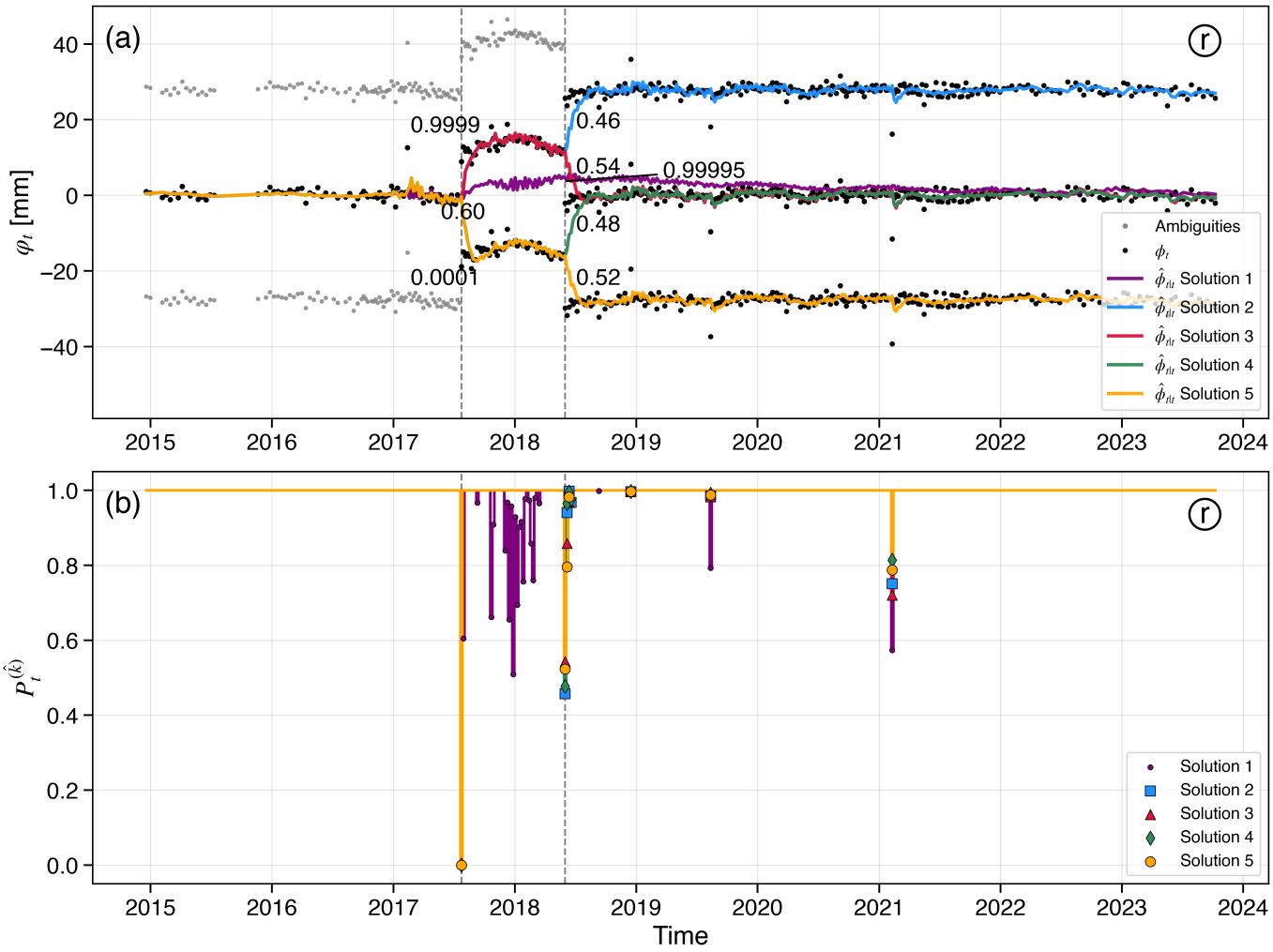


Fig. 8: Comparison of five alternative ISI solutions for the arc shown in Fig. 7. (a) Estimated absolute-phase trajectories, illustrating the bifurcations resulting from alternative integer ambiguity selections in mid-2017 and mid-2018. (b) Corresponding epoch-specific interval probabilities associated with the selected ambiguities. At the first bifurcation, these probabilities are approximately 0.6 for Solution 1, 0.9999 for Solutions 2 and 3, and 0.0001 for Solutions 4 and 5. At the second bifurcation, the probabilities range from approximately 0.46 to 0.54 for Solutions 2–5, whereas Solution 1 retains a probability close to unity. These probabilities characterize individual ambiguity selections under their corresponding prediction models, rather than the probabilities of the complete solution trajectories.

individual decisions were made. For example, Solutions 3 and 4 may appear more plausible when the complete time series is inspected, but this retrospective assessment does not imply that these solutions could have been identified as preferable at the earlier bifurcation epochs.

The results illustrate both the capabilities and limitations of recursive ambiguity resolution. The interval probabilities quantify the discrimination between competing ambiguity candidates using only the information available at each epoch. When this discrimination is weak, the estimator may be unable to identify the correct ambiguity reliably without additional information or assumptions. The resulting uncertainty cannot be eliminated by appealing to future observations that were unavailable at the time of the decision.

B. Influence of the Smoothness Doublet on Ambiguity Discrimination

The postulated smoothness doublet influences the interval probabilities through both the predicted phase residual and its variance. These quantities are coupled because the smoothness doublet determines the state transition and process covariance in the Kalman time update. A smaller σ_v reduces the magnitude of the stochastic velocity fluctuations permitted by the model, whereas τ_v controls their temporal persistence. Consequently, different smoothness doublets produce different predicted states, covariance matrices, and candidate phase residuals.

A relatively restrictive smoothness model may yield a precise prediction during periods of minimal displacement

but produce large predicted residuals when the observed displacement deviates from the assumed dynamics. Conversely, a more flexible model can accommodate greater temporal variability, generally at the expense of increased prediction uncertainty. The interval probability assigned to a candidate therefore depends on the combination of the predicted residual magnitude and its uncertainty, rather than on either quantity independently.

The examples in Fig. 8 illustrate this interaction. At the first phase jump in mid-2017, Solution 1, with a more restrictive smoothness doublet, assigns an interval probability of approximately 0.6 to the selected ambiguity, compared with 0.9999 for Solution 3. Although Solution 1 has a smaller predicted residual variance, its larger residual results in a lower interval probability. At the second phase jump in mid-2018, the corresponding probabilities are approximately 0.99995 and 0.54, respectively. Here, the smaller residual and predicted variance of Solution 1 result in a higher interval probability. These examples demonstrate that a more restrictive model does not necessarily produce higher ambiguity probabilities.

The choice of the smoothness doublet is therefore application dependent. For motion tracking, a sufficiently flexible model is desirable to accommodate the expected temporal variability of displacement. For anomaly detection, a more persistent model may be preferable because departures from the expected dynamics produce larger predicted residuals, and are hence detectable with higher power. The appropriate parameterization consequently depends on the monitoring objective and the acceptable probabilities of false alarms and missed detections.

Thus, the smoothness doublet affects not only the estimated displacement trajectory but also the discrimination between competing integer ambiguity candidates. Its selection should account for both the expected displacement dynamics and the intended application.

C. Influence of Measurement Noise on Ambiguity Discrimination

The measurement-noise variance contributes directly to the predicted phase residual variance and thereby influences the interval probabilities associated with candidate integer ambiguities. The measurement-noise covariance is estimated separately for each acquisition using incremental amplitude time series.

The estimated measurement-noise variances indicate high phase-observation quality before the first bifurcation in mid-2017. The small measurement-noise contribution favors a more concentrated predicted residual distribution, allowing stronger discrimination between neighboring ambiguity candidates. This is reflected in the markedly different interval probabilities associated with Solutions 3 and 5 in Fig. 8.

At the second bifurcation in mid-2018, the phase-observation quality is lower, increasing the measurement-noise contribution to the predicted residual variance. The increased measurement-noise variance contributes to a broader predicted residual distribution, reducing the discrimination between neighboring ambiguity candidates, as illustrated by the comparable interval probabilities for Solutions 2 and 3, and for Solutions 4 and 5. The extent of this discrimination also depends on the predicted state uncertainty and the candidate residuals.

Although the observation quality subsequently improves, this recovery is unknown at the time of the ambiguity decision. Reduced measurement quality can therefore weaken ambiguity discrimination precisely when a decision must be made, without the benefit of future observations.

VI. Conclusions

We presented a probabilistic ambiguity-resolution approach for Instantaneous State InSAR (ISI) that incorporates prior knowledge of displacement dynamics through stochastic smoothness constraints. The approach enables recursive state estimation directly from wrapped phase observations, with integer ambiguity decisions made as each new SAR acquisition becomes available, without requiring future observations.

The smoothness doublet, consisting of the standard deviation and decorrelation time of instantaneous velocity, governs the state prediction and its uncertainty. To facilitate its a priori specification, we introduced two alternative descriptors: the effective fractal dimension, characterizing temporal roughness, and a probabilistic bound on the absolute average velocity over a specified time interval. Relationships between these descriptors and the smoothness doublet were established through simulation and analytical modeling, providing practical guidance for selecting the stochastic model parameters.

In the measurement update, candidate integer ambiguities are evaluated using the predicted phase residual and its variance. Gaussian probability masses assigned to candidate residual intervals provide a quantitative measure of ambiguity discrimination under the postulated stochastic model. The results demonstrate that different ambiguity selections can lead to distinct subsequent displacement trajectories, while the smoothness doublet and measurement noise jointly influence the discrimination between competing candidates. A restrictive smoothness model may improve the precision of the prediction but produce large residuals when the observed displacement deviates from the assumed dynamics.

The results also highlight an inherent limitation of recursive ambiguity resolution: when competing candidates receive comparable probability masses, the correct ambiguity may not be identifiable from the information available at that epoch. The appropriate smoothness doublet therefore depends on the monitoring objective, particularly the distinction between tracking displacement variability and detecting deviations from expected behavior. Developing application-specific criteria for ambiguity discrimination and anomaly detection remains an important direction for future research.

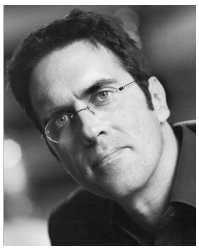
References

[1] Y. Wang, W. S. Brouwer, F. J. van Leijen, and R. F. Hanssen, "Instantaneous State InSAR: Estimation and Prediction for Near Real-Time Displacement Monitoring," *IEEE Transactions on Geoscience and Remote Sensing*, vol. 64, pp. 1–14, 2026.

[2] Y. Wang, W. S. Brouwer, F. J. Van Leijen, and R. F. Hanssen, "Non-parametric InSAR time series analysis of arcs using complex b-splines," in *IEEE International Geoscience and Remote Sensing Symposium (IGARSS)*, 2023, pp. 8238–8241.
[3] Y. Wang, W. S. Brouwer, F. J. van Leijen, and R. F. Hanssen, "Constrained recursive parameter estimation for insar arcs," in *IEEE International Geoscience and Remote Sensing Symposium (IGARSS)*, 2024, pp. 10 689–10 693.
[4] G. E. Uhlenbeck and L. S. Ornstein, "On the theory of the brownian motion," *Physical Review*, vol. 36, pp. 823–841, Sep 1930.
[5] K. Pearson, "The Problem of the Random Walk," *Nature*, vol. 72, no. 1865, p. 294, 1905. [Online]. Available: https://doi.org/10.1038/072294b0
[6] S. Särkkä, *Bayesian Filtering and Smoothing*. Cambridge University Press, 2013.
[7] R. E. Kalman, "A new approach to linear filtering and prediction problems," *Transactions of the ASME–Journal of Basic Engineering*, vol. 82, no. Series D, pp. 35–45, 1960.
[8] R. Bamler and P. Hartl, "Synthetic aperture radar interferometry," *Inverse Problems*, vol. 14, no. 4, pp. R1–R54, 1998.
[9] P. J. G. Teunissen, *Dynamic data processing: Recursive least-squares*, 2nd ed. Delft: TU Delft OPEN Publishing, 2024.
[10] W. S. Brouwer and R. F. Hanssen, "On the definition of an independent stochastic model for InSAR time series," *IEEE Transactions on Geoscience and Remote Sensing*, vol. 63, pp. 1–11, 2025.
[11] P. J. G. Teunissen, "Success probability of integer GPS ambiguity rounding and bootstrapping," *Journal of Geodesy*, vol. 72, no. 10, pp. 606–612, 1998.
[12] ——, "Probabilistic properties of GNSS integer ambiguity estimation," *Earth, Planets and Space*, vol. 52, no. 10, pp. 801–805, 2000.
[13] B. B. Mandelbrot and J. W. Van Ness, "Fractional Brownian motions, fractional noises and applications," *SIAM review*, vol. 10, no. 4, pp. 422–437, 1968.
[14] G. Matheron, "Principles of geostatistics," *Economic Geology*, vol. 58, no. 8, pp. 1246–1266, 12 1963.
[15] E. Kreyszig, *Advanced Engineering Mathematics*, 10th ed. Englewood Cliffs, New Jersey: Wiley, 2018.
[16] A. Papoulis and S. U. Pillai, *Probability, Random Variables, and Stochastic Processes*, 4th ed. McGraw-Hill, 2002.



Yuqing Wang received the M.Sc. degree in Geophysics from Sun Yat-sen University, Zhuhai, China, in 2021. She is currently pursuing the Ph.D. degree with the Delft University of Technology, Delft, The Netherlands. Her research interests include time series analysis, near real-time deformation monitoring and change detection using satellite radar interferometry.



Ramon F. Hanssen (Senior Member, IEEE) received the M.Sc. degree in Geodetic Engineering and the Ph.D. degree (cum laude) from Delft University of Technology, The Netherlands, in 1993 and 2001, respectively. He was with the International Institute for Aerospace Survey and Earth Science (ITC), Stuttgart University, Stuttgart, Germany; the German Aerospace Center (DLR), Weßling, Germany; Stanford University, Stanford, CA, USA, as a Fulbright Fellow; and the Scripps Institution of Oceanography, University of California at San Diego, La Jolla, CA, USA, involved in microwave remote sensing, radar interferometry, signal processing, and geophysical application development. Since 2008, he has been an Antoni van Leeuwenhoek Professor in earth observation with the Delft University of Technology.